Hierarchical Fe₂O₃@Co₃O₄ nanowire array anode for high-performance lithium-ion batteries

Q.Q. Xiong [a], X.H. Xia [b], J.P. Tu [a,*], J. Chen [a], Y.Q. Zhang [a], D. Zhou [a], C.D. Gu [a], X.L. Wang [a]

[a] State Key Laboratory of Silicon Materials, Key Laboratory of Advanced Materials and Applications for Batteries of Zhejiang Province and Department of Materials Science and Engineering, Zhejiang University, Hangzhou 310027, China
[b] Division of Physics and Applied Physics, School of Physical and Mathematical Sciences, Nanyang Technological University, Singapore 637371, Singapore

HIGHLIGHTS

- We prepared Fe₂O₃@Co₃O₄ array by the hydrothermal and sacrificial hydrolysis method.
- The porous Co₃O₄ nanowire act as the core and Fe₂O₃ nanoparticle as the shell layer.
- The electrode shows high capacity, good cycle stability and enhanced rate performance.
- This strategy can be generalized to construct other hybrid nanostructures.

ARTICLE INFO

ABSTRACT

A hierarchically Fe₂O₃@Co₃O₄ nanowire array is prepared by the aid of hydrothermal synthesis and sacrificial hydrolysis method. The obtained nanowire array shows hierarchical porosity and large surface area. The resulted Fe₂O₃@Co₃O₄ nanowire array is evaluated as an anode material for Li ion batteries, which exhibits high capacity and good cycle stability (1005.1 mAh g^{-1} after 50 cycles at a current density of 200 mA g^{-1}) and an excellent rate performance, mainly owing to the unique hierarchical nanowire architecture and an elegant synergistic effect of two electrochemically active materials. The developed strategy can be readily generalized to construct other multifunctional hybrid nanostructures, which will be promising materials for high-performance electrochemical devices.

© 2013 Elsevier B.V. All rights reserved.

1. Introduction

With increasing demand in electric energy storage for electric vehicles and modern electronics, lithium-ion batteries (LIBs) as a fast-developing technology have attracted extensive research interest due to their fascinating advantages of high voltage, high energy density, long cycle life and good environment compatibility [1–13]. The pursuit of high-performance LIB never stops and there are continuous demands to develop LIBs with higher power and energy densities. However, current commercialized graphite anode has a relatively low theoretical capacity of 372 mAh g^{-1}. In the past decades, great efforts have been devoted to seeking for alternative anode materials for LIBs to improve their energy densities. Nowadays, transition metal oxides with variable valence have been widely investigated as candidates in view of their multiple oxidation states to meet the ever-growing performance demands [14–25]. However, the application of transition metal oxides is still hampered by their intrinsic poor electrical conductivity, aggregation of active particles during cycling and large volume variation [26–28]. And there has been limited success in producing well-defined nanostructures with excellent Li storage capabilities and high power density. One promising route is to scrupulously design nanostructured electrodes and smart hybridization of bespoke materials, namely, to combine different active metal oxides into the single electrode to take the advantages of both components and offer special properties through the reinforcement or modification of each other.

Recently, great attention has been paid to hybridize nanostructured transition metal oxides with other active/inactive materials to enhance the electrochemical performance [29–32]. In particular, one-dimensional (1D) nanowire heterostructures arouse considerable research interest due to their rich accessible

* Corresponding author. Tel.: +86 571 87952856; fax: +86 571 87952573.
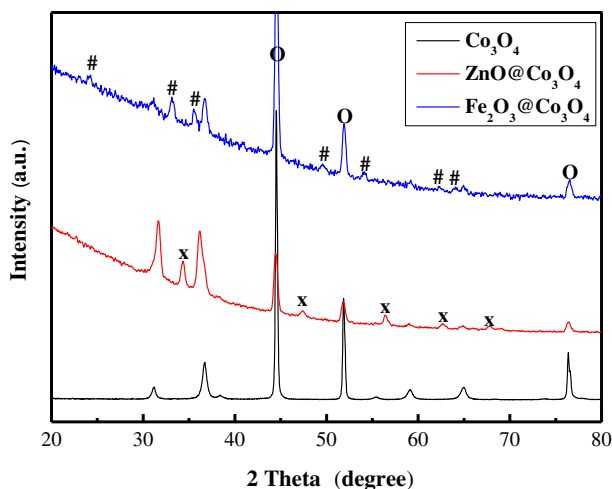E-mail addresses: tujp@zju.edu.cn, tujplab@zju.edu.cn (J.P. Tu).

Fig. 1. XRD pattern of Co_3O_4 nanowire array and $ZnO@Co_3O_4$ and $Fe_2O_3@Co_3O_4$ nanowire array.

electroactive sites, fast Li^+ diffusion and potential synergetic properties or multifunctionalities [30,33–35]. Co_3O_4 and Fe_2O_3, two important members of the metal oxide family, have been the two most widely studied anode materials due to their high theoretical capacity, nontoxicity, and abundance [36–38]. To date, different nanostructures of Co_3O_4 and Fe_2O_3 such as spheres, micro-flowers, nanowires and particles have been synthesized and applied for LIBs. Nevertheless, all these works focus on single Co_3O_4 or Fe_2O_3 electrodes, there are few reports on electrochemical performance of their 1D integrated electrodes by rationally combining merits of Co_3O_4 and Fe_2O_3.

In this present work, we present a simple and cost-effective method to synthesize hierarchical $Fe_2O_3@Co_3O_4$ nanowire array based on the sacrificial template-accelerated hydrolysis mechanism using ZnO as the intermediate template [39], where the porous Co_3O_4 nanowires act as the "core" and ultrathin Fe_2O_3 nanoparticles as the "shell" layer. Impressively, the electrochemical performance of hierarchical $Fe_2O_3@Co_3O_4$ nanowire array is greatly improved with high capacity and excellent cycling life. This enhancement is mainly benefited from the multiple apparent advantages of the nanowire array configuration, such as high surface areas, short ion diffusion path, and direct growth on conductive substrate.

2. Experimental

2.1. Preparation of hierarchical $Fe_2O_3@Co_3O_4$ nanowire array

First, self-supported Co_3O_4 nanowire array was prepared by a typical hydrothermal synthesis method. The solution was prepared by dissolving 0.6 g $Co(NO_3)_2 \cdot 6H_2O$, 0.15 g NH_4F, and 0.6 g $CO(NH_2)_2$ in

75 mL of distilled water. Then the homogeneous solution was transferred into Teflon-lined stainless steel autoclave liners. A piece of clean nickel foam with 3×7 cm^2 in size was immersed into the reaction solution. Its top side of the substrate was uniformly coated with a polytetrafluorethylene tape to prevent the solution contamination. The linear was sealed in a stainless steel autoclave and maintained at 110 °C for 7 h and then annealed at 500 °C for 2 h in Ar.

Then, the nanowire array was synthesized by a simple chemical bath deposition method. The solution was prepared by dissolving 0.6 g $Zn(NO_3)_2 \cdot 6H_2O$, 0.15 g NH_4F, and 0.6 g $CO(NH_2)_2$ in 75 mL of distilled water. Previously prepared film was immersed into the reaction solution at 50 °C for 15 h. Afterward, the sample was annealed at 500 °C in Ar for 2 h.

For the fabrication of $Fe_2O_3@Co_3O_4$ nanowire array, the as-synthesized $ZnO@Co_3O_4$ nanowire array was first placed into a 50 mL solution containing 0.27 g of $Fe(NO_3)_3 \cdot 9H_2O$ and kept still at room temperature for 10 h. After the immersion, it was taken out, dried in air, and treated at 450 °C in Ar for 5 h. The mass ratio of Co_3O_4 and Fe_2O_3 is around 3: 4.

2.2. Characterization

The morphology and microstructure of products were characterized by X-ray diffractometer (XRD, Rigaku D/max 2550 PC, Cu K_α), scanning electron microscopy (SEM, Hitachi S-4700) and transmission electron microscopy (TEM, JEM 200CX at 160 kV, Tecnai G2 F30 at 300 kV).

2.3. Electrochemical investigation

The electrochemical tests were performed using a coin-type half cell (CR 2025). Test cells were assembled in an argon-filled glove box with the metallic lithium foil as the counter electrode, 1 M $LiPF_6$ in ethylene carbonate (EC)-dimethyl carbonate (DME) (1: 1 in volume) as the electrolyte, and a polypropylene (PP) micro-porous film (Cellgard 2300) as the separator. The galvanostatic charge-discharge tests were conducted on a LAND battery program-control test system at certain current densities between 0.01 and 3.0 V at room temperature (25 ± 1 °C). Cyclic voltammetry (CV) was performed on a CHI660C electrochemical workstation in the potential from 0 to 3.0 V (vs. Li^+/Li) at a scanning rate of 0.1 mV s^{-1}. In the electrochemical impedance spectroscopy (EIS) measurement, the excitation voltage applied to the cells was 5 mV and the frequency range was from 100 kHz to 10 mHz. In this experiment, in the term of capacity of the $Fe_2O_3@Co_3O_4$ nanowire array, it is based on the quality of both the active materials.

3. Results and discussion

The crystal structure of the $Fe_2O_3@Co_3O_4$ nanowire arrays is analyzed by XRD, with the result shown in Fig. 1. The composite
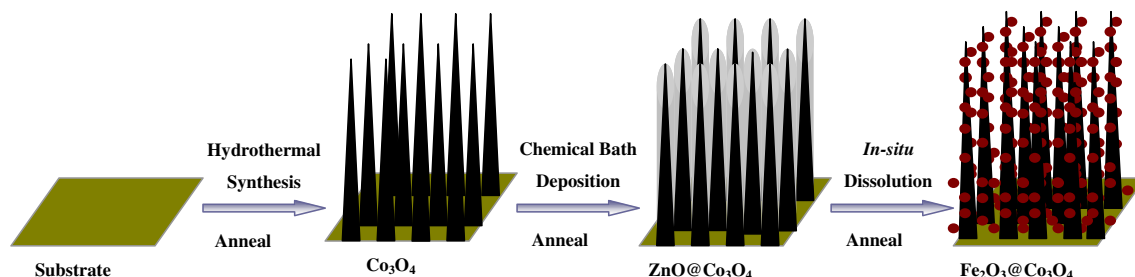

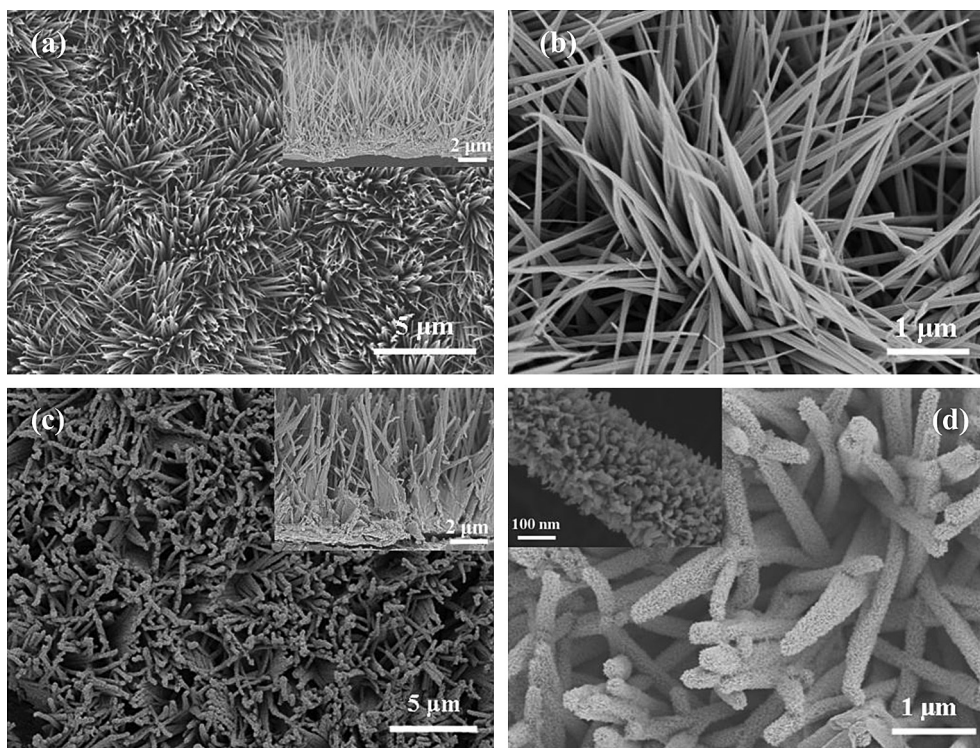**Fig. 2.** A schematic illustration of the formation of hierarchical $Fe_2O_3@Co_3O_4$ nanowire array.

Fig. 3. Top and cross-sectional SEM images of (a, b) Co_3O_4 nanowire array and (c, d) hierarchical $Fe_2O_3@Co_3O_4$ nanowire array.

nanowire array shows a mixed XRD pattern of cubic Co_3O_4 (JCPDF card no. 42-1467) and hexagonal Fe_2O_3 (JCPDF card no. 33-0664). No peaks of other impurity can be observed, suggesting that $Fe(OH)_3$ is completely transformed to Fe_2O_3 after the annealing process. The diffraction peaks at 31.3, 36.9, 38.5, 59.4 and 65.2° are

associated with the 220, 311, 222, 511 and 440 reflections of Co_3O_4, and the diffraction peaks at 24.1, 33.1, 35.6, 49.5, 54.1, 62.4 and 64.0° are correlated to the 012, 104, 110, 024, 116, 214 and 300 reflections of Fe_2O_3, indicating successful synthesis of well-oriented $Fe_2O_3@-Co_3O_4$ nanowire array.
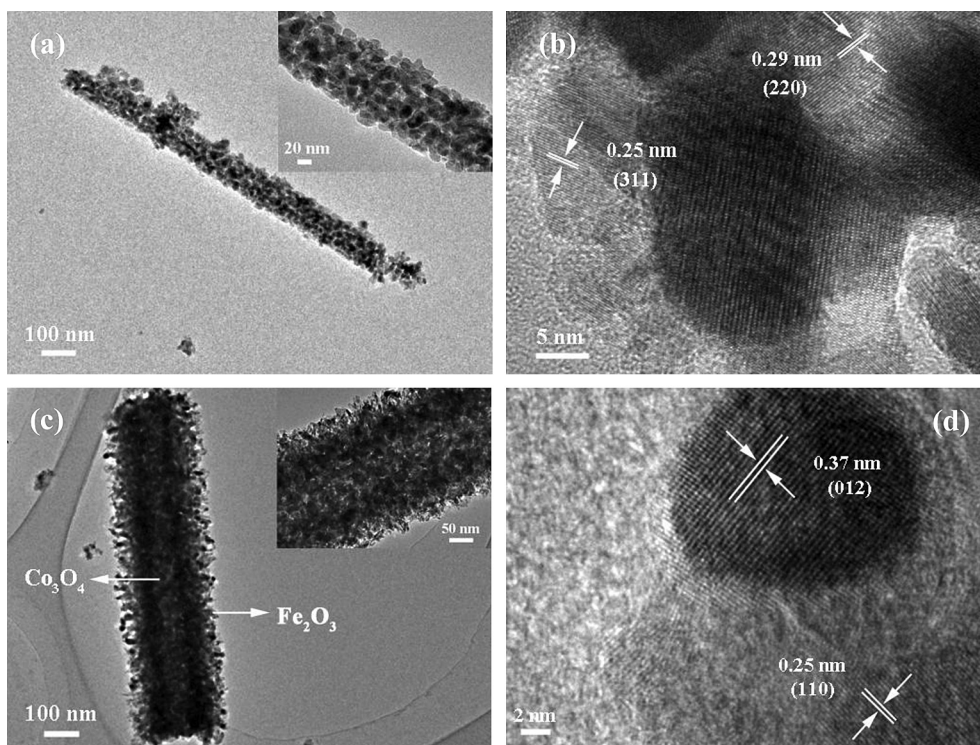

Fig. 4. TEM images of (a) Co_3O_4 nanowire and (b) HRTEM image of Co_3O_4 nanowire and (c) hierarchical $Fe_2O_3@Co_3O_4$ nanowire scratched from Ni foam and (d) HRTEM image of hierarchical $Fe_2O_3@Co_3O_4$ nanowire.
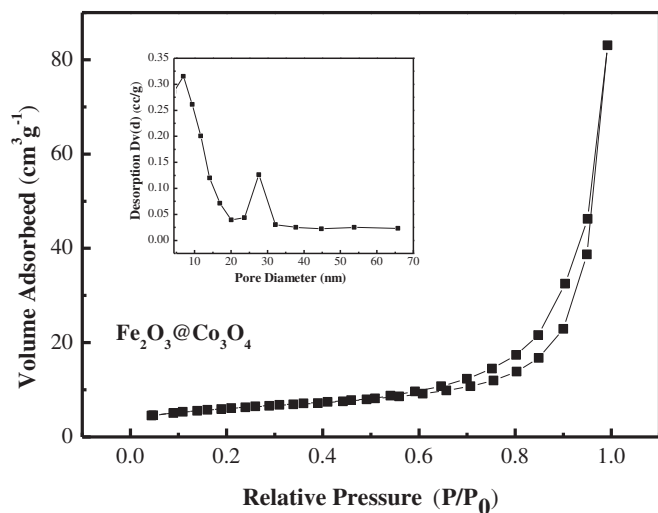
Fig. 5. Nitrogen adsorption−desorption isotherms with corresponding BJH desorption pore size distributions (inset) of hierarchical $Fe_2O_3@Co_3O_4$ nanowire.

Fig. 2 illustrates schematically the formation process of $Fe_2O_3@Co_3O_4$ nanowire array on conductive substrate. The phase purity of samples prepared at different step is illustrated by XRD analysis (Fig. 1). First, Co_3O_4 nanowire arrays are grown on Ni foam

using a typical hydrothermal synthesis method, according to previous works [28,36]. These Co_3O_4 nanowire arrays acting as the backbone, are then subjected to impregnation with Zn^{2+} aqueous solution and subsequent annealing in Ar, which leads to the uniform coating of ZnO layer on the nanowire surface. Herein the ZnO layer is purposely designed as an interfacial reactive template to grow Fe_2O_3 nanostructures. Then, the previously prepared arrays are immersed in an aqueous solution containing Fe^{3+} at room temperature. Simultaneously, the ZnO layer is etched by H^+, which comes from the hydrolysis of Fe^{3+}. As a result, progressive hydrolysis and template dissolution eventually result in the precipitation of $Fe(OH)_3$ emerging on the scaffold of Co_3O_4 nanowire arrays [39]. After this step, the resulting $Fe(OH)_3$ is calcinated in Ar and transformed into ordered $Fe_2O_3@Co_3O_4$ nanowire array. This method provides a new principle for designing integrated nanowire arrays without any porous membranes (AAO or polymers).

The morphologies of the Co_3O_4 nanowire array and $Fe_2O_3@Co_3O_4$ nanowire array are characterized using SEM. Fig. 3a shows the skeletons of the nickel foam are uniformly covered by the slim Co_3O_4 nanowires with diameters of 80−100 nm and length up to around 8 μm, which are homogeneously aligned and separated apart. The top of the Co_3O_4 nanowires is sharp (Fig. 3b). The length of nanowires could be easily controlled by the growth time. With two components integrated, the morphology of the sample does not change much, maintaining the nanowire array structure, but the surface of the composite nanowires becomes a little coarser
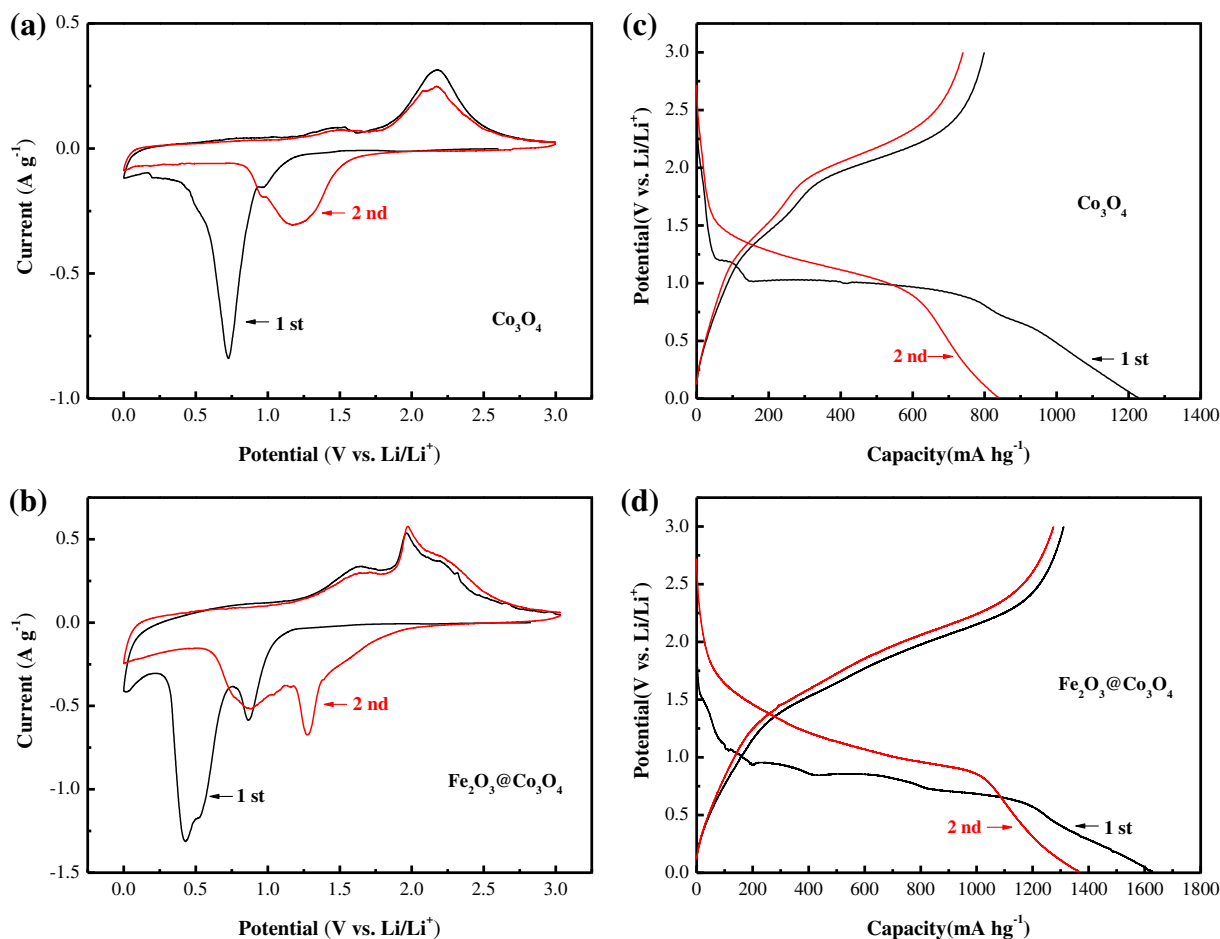

Fig. 6. CV curves of (a) Co_3O_4 nanowire array and (b) hierarchical $Fe_2O_3@Co_3O_4$ nanowire array for the first and second cycles at a scan rate of 0.1 mV s^{-1} in the potential range of 0−3.0 V (versus Li/Li$^+$), and the charge−discharge profiles of (c) Co_3O_4 nanowire array and (d) hierarchical $Fe_2O_3@Co_3O_4$ nanowire array between 0.01 and 3.0 V at a current density of 100 mA g^{-1}.

(Fig. 3c and d). The Co_3O_4 nanowire surface is uniformly decorated by many ultrathin Fe_2O_3 nanoparticles. Thus, nearly all the composite nanowires are highly accessible to electrolytes for energy storage due to the presence of convenient diffusion channels.

The detailed morphological and structural features of the Co_3O_4 nanowire and $Fe_2O_3@Co_3O_4$ nanowire array are also examined by TEM. The Co_3O_4 core nanowire is highly porous, composed of nanocrystallites of 10–20 nm and pores of 4–6 nm (Fig. 4a). The HRTEM examination of a Co_3O_4 nanowire shown in Fig. 4b reveals a distinct set of visible lattice fringes with inter-planar spacing of 0.29 nm and 0.25 nm, corresponding to the (220) and (311) plane of cubic Co_3O_4, respectively. Fig. 4c shows an individual hybrid nanostructure in which ultrathin Fe_2O_3 nanoparticles uniformly cover the surface of the porous Co_3O_4 nanowire. A close examination of the exposed profile reveals that the outer Fe_2O_3 shell is 80–90 nm in thickness. Moreover, the thickness of the Fe_2O_3 shell can be easily varied by controlling the reaction time of Zn^{2+}. The HRTEM image of outer Fe_2O_3 shell shown in Fig. 4d reveals the inter-planar spacing of 0.37 and 0.25 nm, corresponding to the (012) and (110) plane of hexagonal Fe_2O_3. Another phenomenon is that, even after a long time of sonication during the preparation of the TEM specimen, the Fe_2O_3 shell is still strongly attached to the Co_3O_4 nanowire, suggesting the strong interaction of the hybrid nanostructure. The nitrogen adsorption and desorption measurements were performed to estimate the Brunauer–Emmett–Teller (BET) surface area and pore size distribution of the hierarchical $Fe_2O_3@Co_3O_4$ nanowire. As shown in Fig. 5, the isotherm of the hierarchical $Fe_2O_3@Co_3O_4$ nanowire exhibits a hysteresis loop at the P/P_0 ranges of 0.6–1.0, indicating the presence of mesopores. The BET surface area of the hierarchical $Fe_2O_3@Co_3O_4$ nanowire is calculated to be 21.31 m^2 g^{-1}. The plot of pore size distribution determined by the Barrett–Joyner–Halenda (BJH) method (Fig. 5, inset) shows the main pore size of around 6.9 nm and 27.6 nm. The mesopores on the hierarchical nanowire can be attributed to the interspaces of the constituent particles. The result is in good agreement with the value determined by HRTEM observations above. The relatively large specific surface area and porosity offer large materials/electrolyte contact area and promote Li^+ diffusion.

We investigated its ability to reversibly react with lithium in comparison with that of Co_3O_4 nanowire to demonstrate the potential use of hierarchical $Fe_2O_3@Co_3O_4$ nanowire array as an anode for LIBs. Fig. 6a and b show the CV curves of the Co_3O_4 nanowire and $Fe_2O_3@Co_3O_4$ nanowire arrays for the first two cycles in the potential range from 3.0 to 0.0 V (vs. Li/Li$^+$) at ambient temperature at a scan rate of 0.1 mV s^{-1}, respectively. Apparently, a pair of redox peaks is observed for the Co_3O_4 nanowire array electrode, corresponding to the extraction and insertion of lithium ions. The reduction peak corresponds to a multistep electrochemical reaction of Co^{3+} to Co^{2+} and metal Co^0. In the anodic scan, one broad peak in the range of 2–2.5 V is recorded, which is ascribed to the reversible oxidation of metal Co to cobalt oxide [28,40]. For the $Fe_2O_3@Co_3O_4$ nanowire array, it is remarkable that in addition to the peaks from Co_3O_4, indicating the efficient utilization of the underlying Co_3O_4 nanowire despite covered by the Fe_2O_3 nanoparticles, there is another pair of redox peaks (Fig. 6b). The reduction peak at about 0.5 V is observed in the first cathodic scan, which can be attributed to the reduction of Fe^{3+} to Fe^0 and the irreversible reaction with the electrolyte. Meanwhile, the anodic peak at about 1.6 V corresponds to the reversible oxidation of Fe^0 to Fe^{3+}, which agrees well with early studies [41–44]. It is interesting that the area integrated within the current−potential curves greatly increases for the $Fe_2O_3@Co_3O_4$ nanowire array electrode, leading to a much larger capacity. Fig. 6c and d show the first two galvanostatic charge−discharge curves for the two electrodes between 0.01 and 3.0 V at a current density of 100 mA g^{-1}. The $Fe_2O_3@Co_3O_4$ nanowire array
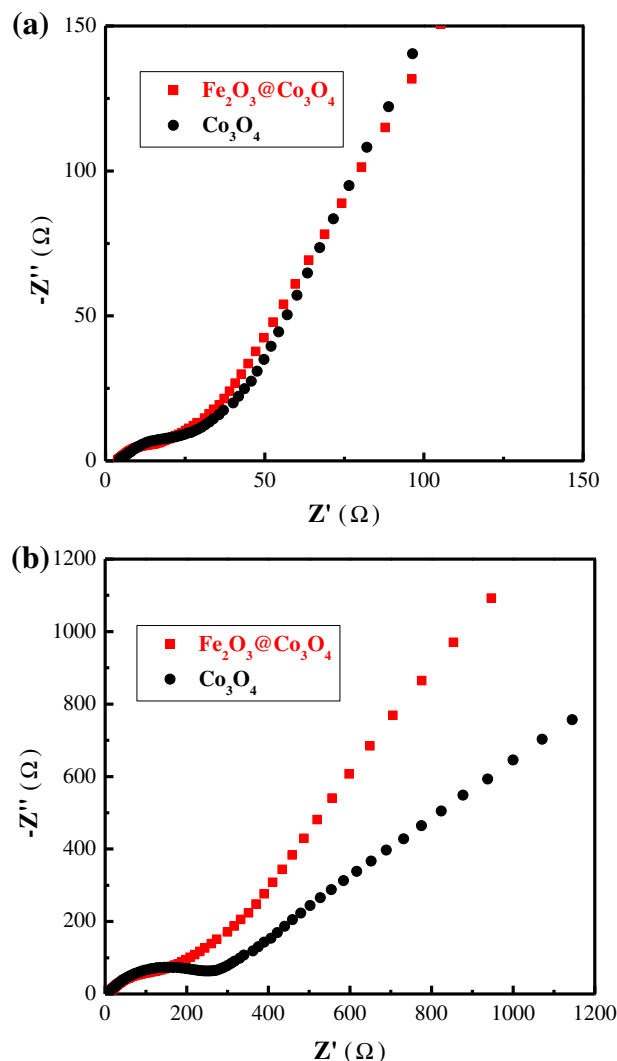
Fig. 7. Nyquist plots of Co_3O_4 nanowire array and (b) hierarchical $Fe_2O_3@Co_3O_4$ nanowire array after (a) 3 cycles and (b) 50 cycles in the frequency range from 100 kHz to 10 mHz.
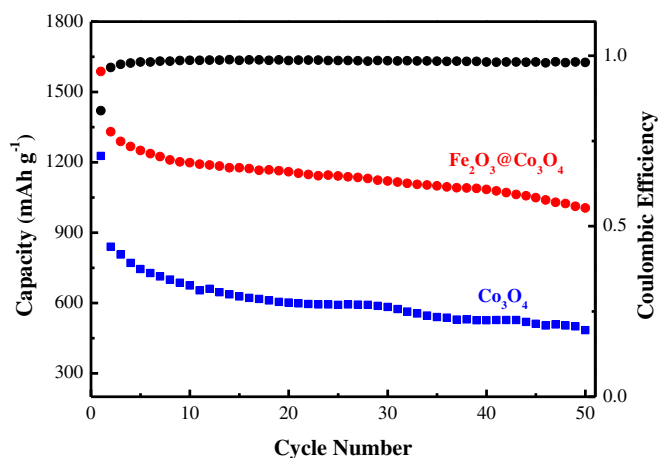
Fig. 8. Cycling performance of Co_3O_4 nanowire and hierarchical $Fe_2O_3@Co_3O_4$ nanowire array electrodes at a current density of 200 mA g^{-1}.

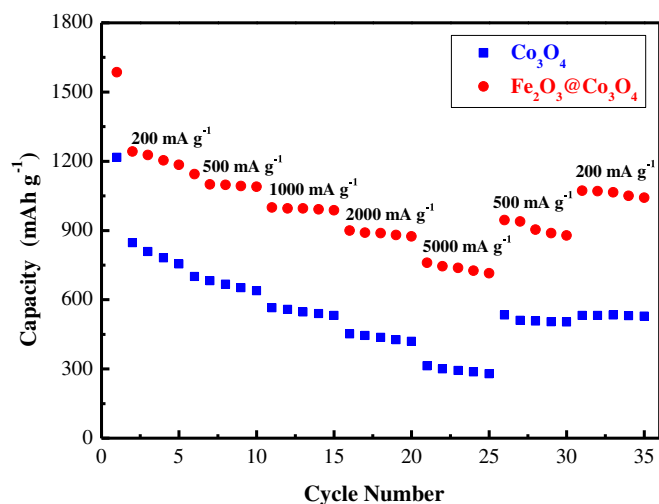**Fig. 9.** Rate performance of Co_3O_4 nanowire array and hierarchical $Fe_2O_3@Co_3O_4$ nanowire array at current density of 200 mA g^{-1} to 5000 mA g^{-1}.

reaches a high initial discharge capacity of 1586.9 mAh g^{-1}, substantially better than that of Co_3O_4 nanowire array (1226.7 mAh g^{-1}). These values are much higher than the theoretical capacity, which can be attributed to be the formation of solid electrolyte interphase (SEI) films on the nanowire arrays during the discharge process [45]. The discharge capacity of two electrodes drops at the second cycle, corresponding to an irreversible capacity loss due to the formation of SEI films, the decomposition of electrolyte and the formation of the irreversible Li_2O [43]. However, the $Fe_2O_3@Co_3O_4$ nanowire array electrode shows smaller irreversible capacity, indicating that the hierarchical nanowire array leads to better reversibility in the charge–discharge processes.

EIS test was also carried out to prove the good performance of hierarchical nanowire array. Fig. 7a shows the Nyquist plots of both the electrodes at room temperature in the frequency range of 100 KHz to 10 mHz after 3 cycles in the fully charged state. They have the same shapes of Nyquist plots, composed of a depressed semicircle where a high-frequency semicircle and a medium-frequency semicircle overlap each other and a long low-frequency line. The intercept on the Z real axis in the high-frequency region corresponds to the resistance of electrolyte (R_s). The semicircle in the middle frequency range indicates the charge-transfer resistance (R_{ct}), relating to charge transfer through the electrode/electrolyte interface. The inclined line in the low-frequency region represents the Warburg impedance (Z_W), which is related to solid-state diffusion of Li$^+$ in the electrode materials [46]. As one can observe that

after 3 cycles, there are no obvious changes of semicircle between the two electrodes. Fig. 7b presents the Nyquist plots of the electrodes after 50 cycles. Obviously, the $Fe_2O_3@Co_3O_4$ nanowire array electrode has smaller semicircle than the Co_3O_4 nanowire array. Therefore, it is suggested that the interparticle resistance of the electrode is suppressed by the hierarchical nanostructure, and consequently, the value of R_{ct} for the $Fe_2O_3@Co_3O_4$ nanowire array electrode is smaller than that of the Co_3O_4 nanowire, indicating that the composite nanowire arrays are beneficial to enhance the reaction kinetics and better cycling performance of the cells during the charge/discharge process.

Fig. 8 shows the cyclability of the Co_3O_4 nanowire and $Fe_2O_3@Co_3O_4$ nanowire array electrodes at a current density of 200 mA g^{-1}. The specific reversible capacity of $Fe_2O_3@Co_3O_4$ nanowire arrays after 50 cycles is 1005.1 mAh g^{-1}, which is much higher than that of Co_3O_4 nanowire (483.9 mAh g^{-1}). The reversible capacity of the $Fe_2O_3@Co_3O_4$ nanowire array remained almost constant since the third cycle, with coulombic efficiency above 98% from the 5th cycle. After 50 cycles, the $Fe_2O_3@Co_3O_4$ nanowire array could sustain 75.6% capacity of the 2nd cycle, compared with 57.7% for Co_3O_4 nanowire array. The substantial enhancement of Li$^+$ storage capacity and stability of hybrid nanowire array is attributed to its composite nanostructure, which provides a short ion diffusion path, maintains the structural integrity of the core by wrapped Fe_2O_3 nanoparticles. In addition, both the Fe_2O_3 and Co_3O_4 are active materials to reversibly undergo redox reactions with Li, hence contributing to high Li$^+$ storage capacity.

In addition to the improved cycling performance, the $Fe_2O_3@Co_3O_4$ nanowire array also show significantly enhanced rate performance compared with the Co_3O_4 nanowire (Fig. 9). The specific capacities of $Fe_2O_3@Co_3O_4$ nanowire array at different charge–discharge current densities are always higher than those of Co_3O_4 nanowire. With increasing the current density from 200 mA g^{-1} to 5000 mA g^{-1}, the discharge capacities of the two electrodes decrease gradually, indicating the diffusion-controlled kinetics process for the electrode reaction. At a current density as high as 5000 mA g^{-1}, the $Fe_2O_3@Co_3O_4$ nanowire array electrode is capable of delivering a stable capacity of about 760.0 mAh g^{-1} after 20 cycles of variable charging rate. Upon decreasing the current density to 200 mA g^{-1}, nearly 84.5% of the capacity of the second cycle at 200 mA g^{-1} (about 1050.0 mAh g^{-1}) can be recovered. Fig. 10 shows the SEM images of the Co_3O_4 and hierarchical $Fe_2O_3@Co_3O_4$ nanowire arrays after 10 cycles at a current density of 200 mA g^{-1}. The surface of $Fe_2O_3@Co_3O_4$ nanowire array is much rougher (Fig. 10b). Fortunately, the ultrathin Fe_2O_3 nanoparticles attaching to the Co_3O_4 nanowire almost exhibit no agglomeration. The morphology of $Fe_2O_3@Co_3O_4$ nanowire array remains well after the lithiation/delithiation cycles, compares to that of Co_3O_4
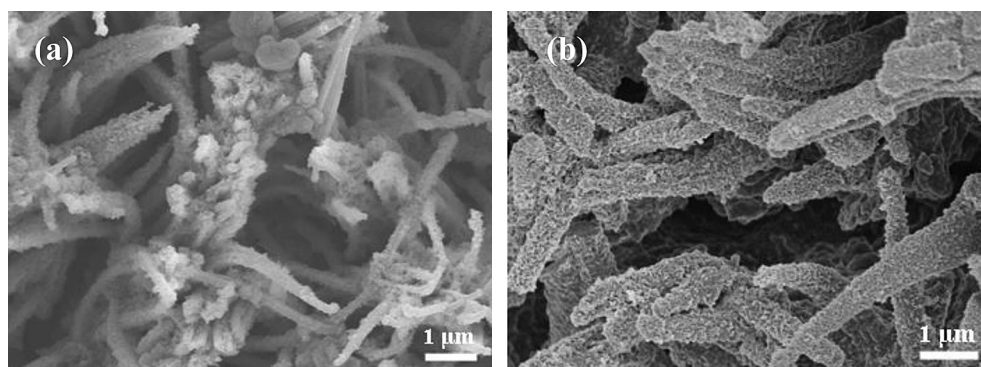

Fig. 10. SEM images of Co_3O_4 nanowire array and hierarchical $Fe_2O_3@Co_3O_4$ nanowire array after 10 cycles at a current density of 200 mA g^{-1}.

(Fig. 10a), indicating that hierarchical nanowire array structure is beneficial to relax the volume expansion and alleviates the structure damage during cycling. The composite array directly grown on conductive Ni foam and the structural stability during cycling may be responsible for the enhanced rate performance, which implying that it is a promising anode material for high energy or high power density LIBs.

4. Conclusions

In summary, we have successfully fabricated hierarchical Fe_2O_3@Co_3O_4 nanowire array based on the sacrificial template-accelerated hydrolysis mechanism using ZnO as the intermediate template. The Fe_2O_3@Co_3O_4 nanowire array exhibits good cycling performance (1005.1 mAh g^{-1} after 50 cycles at 200 mA g^{-1}) and improved rate performance (788.9 mAh g^{-1} at 5000 mA g^{-1}). Such intriguing capacity behavior is attributed to the hierarchical composite nanowire array configuration and the synergistic effects of the combined electrochemical contributions from the Co_3O_4 nanowire core and the ultrathin Fe_2O_3 nanoparticle shell. The utilization of advanced hierarchical integrated array structure is suggested as a promising strategy toward the development of transition metal oxides as high-performance electrode materials for LIBs.

Acknowledgments

References

[1] J.M. Tarascon, M. Armand, Nature 414 (2001) 359.
[2] A.S. Arico, P. Bruce, B. Scrosati, J.M. Tarascon, W. Van Schalkwijk, Nat. Mater. 4 (2005) 366.
[3] M. Armand, J.M. Tarascon, Nature 451 (2008) 652.
[4] Y.J. Mai, S.J. Shi, D. Zhang, Y. Lu, C.D. Gu, J.P. Tu, J. Power Sources 204 (2012) 155.
[5] A. Brandt, A. Balducci, J. Power Sources 230 (2013) 44–49.
[6] J.Y. Xiang, J.P. Tu, L. Zhang, Y. Zhou, X.L. Wang, S.J. Shi, Electrochim. Acta 55 (2010) 1820.
[7] V. Aravindan, P.S. Kumar, J. Sundaramurthy, W.C. Ling, S. Ramakrishna, S. Madhavi, J. Power Sources 227 (2013) 284.
[8] Y. Lu, J.-P. Tu, Q.-Q. Xiong, J.-Y. Xiang, Y.-J. Mai, J. Zhang, Y.-Q. Qiao, X.-L. Wang, C.-D. Gu, S.X. Mao, Adv. Funct. Mater. 22 (2012) 3927.
[9] J.J. Zhang, Y.F. Sun, Y. Yao, T. Huang, A.S. Yu, J. Power Sources 222 (2013) 59.
[10] M. Sathish, T. Tomai, I. Honma, J. Power Sources 217 (2012) 85.
[11] Y. Lu, J.-P. Tu, Q.-Q. Xiong, H. Zhang, C.-D. Gu, X.-L. Wang, S.X. Mao, Cryst Eng. Comm. 14 (2012) 8633.
[12] D. Zhang, X.L. Wang, Y.J. Mai, X.H. Xia, C.D. Gu, J.P. Tu, J. Appl. Electrochem 42 (2012) 263.
[13] J. Shu, L. Hou, R. Ma, M. Shui, L.Y. Shao, D.J. Wang, Y.L. Ren, W.D. Zheng, RSC Adv. 2 (2012) 10306.
[14] B. Wang, J.S. Chen, H.B. Wu, Z.Y. Wang, X.W. Lou, J. Am. Chem. Soc. 133 (2011) 17146.
[15] W.D. Zhang, W. Wan, H.H. Zhou, J.T. Chen, X.Y. Wang, X.X. Zhang, J. Power Sources 223 (2013) 119.
[16] Y.J. Mai, J.P. Tu, X.H. Xia, C.D. Gu, X.L. Wang, J. Power Sources 196 (2011) 6388.
[17] B.G. Choi, S.-J. Chang, Y.B. Lee, J.S. Bae, H.J. Kim, Y.S. Huh, Nanoscale 4 (2012) 5924.
[18] X.H. Xia, J.P. Tu, Y.Q. Zhang, J. Chen, X.L. Wang, C.D. Gu, C. Guan, J.S. Luo, H.J. Fan, Chem. Mater. 24 (2012) 3793.
[19] M.E. Donders, H.C.M. Knoops, W.M.M. Kessels, P.H.L. Notten, J. Power Sources 203 (2012) 72.
[20] L. Chang, L.Q. Mai, X. Xu, Q.Y. An, Y.L. Zhao, D.D. Wang, X. Feng, RSC Adv. 3 (2013) 1947.
[21] R.H. Wang, C.H. Xu, J. Sun, L. Gao, C.C. Lin, J. Mater. Chem. A 1 (2013) 1794.
[22] J.Y. Xiang, X.L. Wang, X.H. Xia, L. Zhang, Y. Zhou, S.J. Shi, J.P. Tu, Electrochim. Acta 55 (2010) 4921.
[23] H. Kitamura, L. Zhao, B.T. Hang, S. Okada, J.-I. Yamaki, J. Power Sources 208 (2012) 391.
[24] W. Tang, X.W. Gao, Y.S. Zhu, Y.B. Yue, Y. Shi, Y.P. Wu, K. Zhu, J. Mater. Chem. 22 (2012) 20143.
[25] B. Wang, J.L. Cheng, Y.P. Wu, D. Wang, D.N. He, Electrochem. Commun. 23 (2012) 5.
[26] Q.Q. Xiong, J.P. Tu, Y. Lu, J. Chen, Y.X. Yu, Y.Q. Qiao, X.L. Wang, C.D. Gu, J. Phys. Chem. C 116 (2012) 6495.
[27] Z.Y. Wang, D.Y. Luan, S. Madhavi, C.M. Li, X.W. Lou, Chem. Commun. 47 (2011) 8061.
[28] J. Chen, X.H. Xia, J.P. Tu, Q.Q. Xiong, Y.X. Yu, X.L. Wang, C.D. Gu, J. Mater. Chem. 22 (2012) 15056.
[29] Y. Qi, N. Du, H. Zhang, X. Fan, Y. Yang, D.R. Yang, Nanoscale 4 (2012) 991.
[30] X.H. Xia, J.P. Tu, Y.Q. Zhang, X.L. Wang, C.D. Gu, X.B. Zhao, H.J. Fan, ACS Nano 6 (2012) 5531.
[31] J.P. Liu, J. Jiang, C.W. Cheng, H.X. Li, J.X. Zhang, H. Gong, H.J. Fan, Adv. Mater. 23 (2011) 2076.
[32] S. Jung, K. Yong, Chem. Commun. 47 (2011) 2643.
[33] X.H. Lu, T. Zhai, X.H. Zhang, Y.Q. Shen, L.Y. Yuan, B. Hu, L. Gong, J. Chen, Y.H. Gao, J. Zhou, Y.X. Tong, Z.L. Wang, Adv. Mater. 24 (2012) 938.
[34] J.P. Liu, J. Jiang, M. Bosman, H.J. Fan, J. Mater. Chem. 22 (2012) 2419.
[35] H. Jiang, C.Z. Li, T. Sun, J. Ma, Chem. Commun. 48 (2012) 2606.
[36] X.H. Xia, J.P. Tu, Y.Q. Zhang, Y.J. Mai, X.L. Wang, C.D. Gu, X.B. Zhao, RSC Adv. 2 (2012) 1835.
[37] J.P. Liu, Y.Q. Song, S.S. Qin, Y.W. Zhang, W.Q. Gao, J. Phys. Chem. C 114 (2010) 21158.
[38] J.S. Chen, C.M. Li, W.W. Zhou, Q.Y. Yan, L.A. Archerc, X.W. Lou, Nanoscale 1 (2009) 280.
[39] J.P. Liu, Y.Y. Li, H.J. Fan, Z.H. Zhu, J. Jiang, R.M. Ding, Y.Y. Hu, X.T. Huang, Chem. Mater. 22 (2010) 212.
[40] D. Larcher, G. Sudant, J.B. Leriche, Y. Chabre, J.M. Tarascon, J. Electrochem. Soc. 149 (2002) A234.
[41] H. Liu, G.X. Wang, J. Park, J. Wang, H. Liu, C. Zhang, Electrochim. Acta 54 (2009) 1733.
[42] K.L. Huang, F. Cheng, S.Q. Liu, J.L. Liu, R.J. Deng, Electrochim. Acta 56 (2011) 5593.
[43] S.-L. Chou, J.-Z. Wang, D. Wexler, K. Konstantinov, C. Zhong, H.-K. Liu, S.-X. Dou, J. Mater. Chem. 20 (2012) 2092.
[44] X.W. Guo, X. Lu, X.P. Fang, Y. Mao, Z.X. Wang, L.Q. Chen, X.X. Xu, H. Yang, Y.N. Liu, Electrochem. Commun. 12 (2010) 847.
[45] Q.Q. Xiong, J.P. Tu, Y. Lu, J. Chen, Y.X. Yu, X.L. Wang, C.D. Gu, J. Mater. Chem. 22 (2012) 18639.
[46] J.Y. Xiang, J.P. Tu, Y.Q. Qiao, X.L. Wang, J. Zhong, D. Zhang, C.D. Gu, J. Phys. Chem. C 115 (2011) 2505.